Dalton Transactions

ROYAL SOCIETY OF CHEMISTRY

PAPER

View Article Online
View Journal | View Issue

Cite this: *Dalton Trans.*, 2020, **49**, 343

Copper-based redox shuttles supported by preorganized tetradentate ligands for dye-sensitized solar cells†

Roberta R. Rodrigues, Joseph M. Lee, Natalie S. Taylor, Hammad Cheema, Lizhu Chen, Ryan C. Fortenberry,* Jared H. Delcamp* and Jonah W. Jurss*

Received 14th October 2019,
Accepted 1st December 2019

DOI: 10.1039/c9dt04030g

rsc.li/dalton

Three copper redox shuttles ($[Cu(\mathbf{1})]^{2+/1+}$, $[Cu(\mathbf{2})]^{2+/1+}$, and $[Cu(\mathbf{3})]^{2+/1+}$) featuring tetradentate ligands were synthesized and evaluated computationally, electrochemically, and in dye-sensitized solar cell (DSC) devices using a benchmark organic dye, **Y123**. Neutral polyaromatic ligands with limited flexibility were targeted as a strategy to improve solar-to-electrical energy conversion by reducing voltage losses associated with redox shuttle electron transfer events. Inner-sphere electron transfer reorganization energies (λ) were computed quantum chemically and compared to the commonly used $[Co(bpy)_3]^{3+/2+}$ redox shuttle which has a reported λ value of 0.61 eV. The geometrically constrained biphenyl-based Cu redox shuttles investigated here have lower reorganization energies (0.34–0.53 eV) and thus can potentially operate with lower driving forces for dye regeneration (ΔG_{reg}) in DSC devices when compared to $[Co(bpy)_3]^{3+/2+}$-based devices. The rigid tetradentate ligand design promotes more efficient electron transfer reactions leading to an improved J_{SC} (14.1 mA cm^{-2}), higher stability due to the chelate effect, and a decrease in V_{OC}^{loss} for one of the copper redox shuttle-based devices.

Introduction

Dye-sensitized solar cells (DSCs) are relatively inexpensive and highly-processable photovoltaic devices that allow direct conversion of sunlight-to-electrical energy.[1–10] DSC devices are comprised of a semiconductor (typically TiO_2) decorated with surface-bound dye molecules which inject electrons into the semiconductor upon photoexcitation in a functional device. A redox shuttle (RS) then reduces the oxidized dye and collects the injected electrons from a counter electrode after the electrons have traversed an external circuit. The RS plays critical roles in controlling DSC device efficiencies and stabilities by dictating the maximum open-circuit voltage that can be obtained (the energetic distance between the TiO_2 conduction band (CB) and the standard potential of the RS). The RS also controls the efficiencies of key electron transfer processes to the dye and from the counter electrode.[3,10–14]

Recent efforts have focused on diminishing the free-energy driving force for electron transfer from the RS to the dye and accessing energetically tunable RSs to enable matching of RSs to dye energetics.[15] These results have led to the replacement of the classically used two-electron transfer iodide/triiodide (I^-/I_3^-) redox shuttle with suitable transition metal complexes that serve as one-electron transfer mediators in high efficiency devices, which has raised efficiencies from record literature values of about 11% with I^-/I_3^- to >14% with a Co^{3+}/Co^{2+} RS.[16–18,19] Recently, $Cu^{2+/1+}$ redox shuttles[10,15,20–37] have shown considerable promise with reported efficiencies in excess of 13%[25] and impressively low driving forces for dye regeneration (ΔG_{reg}) near 150 mV.[15] Interestingly, Cu-based devices are also reported to have improved performance as solid state systems with high efficiencies where the Cu RS plays the role of a hole-transport material (HTM).[21,24,25] These unusual behaviors have sparked significant interest in copper redox shuttle designs to probe the effects of the ligand on device performances.

The ΔG_{reg} needed in DSC devices with transition metal-based RSs is related to the inner-sphere reorganization energy (λ) required of the complex to change the oxidation state of the metal center.[22] This represents an energetic barrier which is often overcome by increasing ΔG_{reg} values; however, this leads to: (1) a loss of maximum open circuit voltage (V_{OC}) by shifting the RS potential closer to the TiO_2 conduction band (CB) energy, or (2) a lower maximum short-circuit current density (J_{SC}) by requiring a wider optical gap dye with a positive ground state oxidation potential (Fig. 1). As a result lower

Department of Chemistry and Biochemistry, University of Mississippi, University, MS 38677, USA. E-mail: jwjurss@olemiss.edu, delcamp@olemiss.edu, r410@olemiss.edu

†Electronic supplementary information (ESI) available. CCDC 1959279. For ESI and crystallographic data in CIF or other electronic format see DOI: 10.1039/c9dt04030g

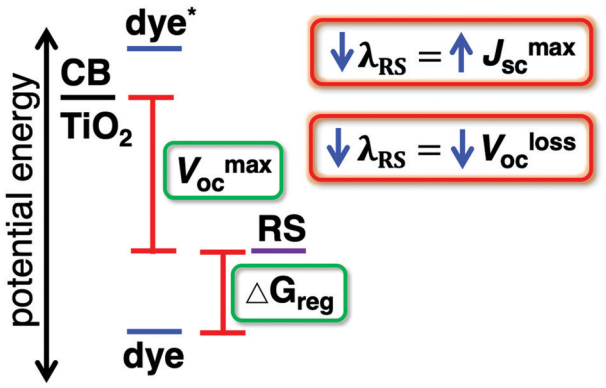

Fig. 1 Energy diagram illustrating the relationship of the TiO_2 CB, RS oxidation potential, and ΔG_{reg} as the free energy driving force for regeneration. Decreasing λ decreases the required ΔG_{reg} needed.

overall solar cell power conversion efficiencies (η) are possible when ΔG_{reg} values are high.[15] Many of the reported Cu-based RSs are limited to bidentate ligands, which enable flexible coordination environments about the metal and potentially higher electron transfer reorganization energies. The design of a rigid, preorganized tetradentate ligand framework could reduce reorganization energies significantly and allow smaller ΔG_{reg} values.[20,26]

Inspiration for the tetradentate ligand design approach is found both in nature and in model systems.[38–45] For example, several biphenyl-based ligands have been used to model blue copper protein active sites.[39–43] Metalloenzymes, such as plastocyanin and azurin, exhibit fast electron transfer kinetics, which is thought to arise from the low inner-sphere reorganization energy associated with their nearly isostructural Cu(II/I) redox states.[39–43] The model systems employing biphenyl exploit the substituted phenyl groups as a rigid structural unit that allows the appended donors to chelate to a single metal center while forcing the nitrogen donor atoms into a pseudo-tetrahedral arrangement and preventing access to the favored square planar geometry of Cu(II).[46] With this approach, three tetradentate ligated Cu complexes were targeted for comparison to a benchmark Cu RS bearing bidentate 1,1-bis(2-pyridyl) ethane (bpye) ligands, $[Cu(bpye)_2]^{2+/1+}$,[21] and evaluated computationally, electrochemically, and in DSC devices using a benchmark organic dye, **Y123**[22] (Fig. 2). The rigid biphenyl-bridged tetradendate ligands investigated here feature tunable bidentate donor fragments, namely bipyridine donors in $[Cu(\mathbf{1})]^{2+/1+}$,[39,46] pyridyl-methyltriazole donors in $[Cu(\mathbf{2})]^{2+/1+}$,[42] and trifluoromethylpyridyl-methyltriazole donors in $[Cu(\mathbf{3})]^{2+/1+}$. This family of ligands allows for the probing of Cu-RS properties with varied bond angles, for example, between adjacent N–Cu–N bonds as dictated by having two 6-membered heterocyclic donors with bipyridine or both 5- and 6-membered heterocycles with the pyridyl-triazole units. Additionally, the tunability of the RS potential energy through the use of electron withdrawing CF_3 groups is evaluated.

Results and discussion

Redox shuttles $[Cu(\mathbf{1})]^{2+/1+}$ and $[Cu(\mathbf{2})]^{2+/1+}$ were synthesized according to known procedures for these complexes.[39,42,46] $[Cu(\mathbf{3})]^{2+/1+}$ is a new pair of complexes which were synthesized from starting material **1** (Scheme 1). Commercially available cyano-substituted pyridine **1** was reacted with methylhydrazine to generate the trifluoromethyl-functionalized amidrazone (**2**) in up to 55% yield. Ligand **3** was obtained by stirring the amidrazone intermediate **2** with diphenic acyl chloride[42] and heating the product to cyclize the triazole fragment in quantitative yield. Finally, an equimolar ratio of the appropriate copper salt (either $[Cu(MeCN)_4](PF_6)$ or $[Cu(ClO_4)_2]\cdot 6H_2O$) and

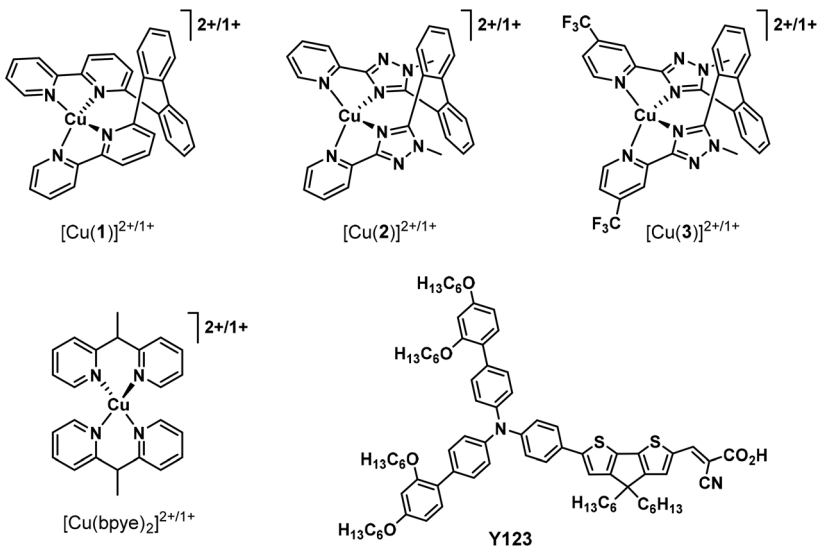

Fig. 2 Structures of $[Cu(\mathbf{1})]^{2+/1+}$, $[Cu(\mathbf{2})]^{2+/1+}$, $[Cu(\mathbf{3})]^{2+/1+}$, $[Cu(bpye)_2]^{2+/1+}$, and **Y123**.

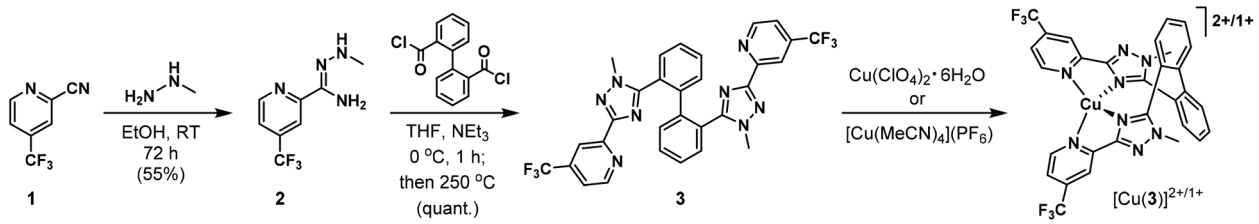

Scheme 1 Synthesis of the CF_3-substituted biphenyl-based copper(II/I) redox shuttles.

ligand **3** were stirred to afford copper compounds $[Cu(\mathbf{3})]^{1+}$ and $[Cu(\mathbf{3})]^{2+}$, respectively.

In order to test our hypothesis that rigid preorganized ligands could improve device efficiencies, the inner-sphere reorganization energy (λ) associated with each system was investigated computationally and *via* crystallographic data by analyzing the geometry changes that occur upon changing the oxidation state of the Cu center. In the case of $[Cu(\mathbf{1})]^{1+}$, crystallographic values are available in the literature for comparison to computed values; however, $[Cu(\mathbf{1})]^{2+}$ values were not available due to the reported Cu(II) structure being a 5-coordinate species with a bound chloride donor.[39] Chloride was removed in the present study and crystals of the Cu(II) species with perchlorate counter anions were grown from acetonitrile by slow diethyl ether diffusion into the solution. The crystal structure is shown in Fig. 3 where the Cu(II) complex possesses a 5-coordinate geometry with a bound acetonitrile donor and a weakly associated perchlorate ion. The nearest oxygen (O4) of the perchlorate anion is 2.9033(12) Å from copper, which is significantly longer than the sum of their covalent radii and roughly equal to the sum of their van der Waals radii (a measure of the contact distance between unbonded atoms). Moreover, assuming a 6-coordinate species, the pyridine *trans* to the associated perchlorate anion has a Cu–N3 bond distance of 2.2525(10) Å and is bent away from the metal and is not coplanar with the adjacent pyridine. These distances are consistent with Jahn–Teller distortion where the remaining Cu–N bond distances involving N1, N2, N4, and N5 have an average length of 2.02 Å. In addition, crystal structures of both the reduced and oxidized complexes of $[Cu(\mathbf{2})]^{2+/1+}$ have been reported.[42] Notably, the crystals for this system were also grown from acetonitrile solutions and 4-coordinate copper complexes were observed for both oxidation states.

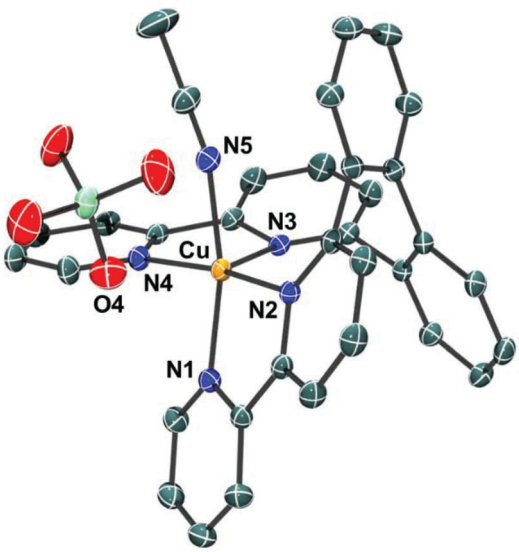

Fig. 3 Crystal structure of $[Cu(\mathbf{1})(MeCN)](ClO_4)_2$ with thermal ellipsoids rendered at 50% probability level. Hydrogen atoms have been omitted for clarity. One of the two perchlorate anions is shown due to its weak interaction with the Cu(II) metal center (Cu···O4 distance = 2.9033(12) Å).

With crystallographic data in hand, the inner-sphere λ values were assessed computationally with density functional theory (DFT) approaches as shown previously for $Cu^{2+/1+}$ redox systems.[22] Here, λ represents the difference in the energy for the 2+ oxidation state computed at the 1+ optimized geometry and the energy at the optimized 2+ oxidation state geometry.[47] Using a similar approach to that previously reported for redox shuttle $[Cu(dmby)_2]^{2+/1+}$ (where dmby is 6,6′-dimethyl-2,2′-bipyridine), the reorganization energies for each of the Cu RSs were analyzed *via* the PBE1PBE (PBE0)[48,49] and B3PW91[50,51] functionals within the Gaussian09[52] program employing a polarizable continuum solvent model for acetonitrile. The 6-31G(d) basis set[53] was used for all atoms except Cu where Def2TZVP[54,55] was employed.

In the case of the biphenyl-based ligands used in complexes $[Cu(\mathbf{1})]^{2+/1+}$, $[Cu(\mathbf{2})]^{2+/1+}$, and $[Cu(\mathbf{3})]^{2+/1+}$, the inner-sphere λ values were limited to 0.34–0.53 eV (Table 1, entries 1–4). $[Cu(\mathbf{1})]^{2+/1+}$ has the smallest λ value of the series at 0.34 eV with either method indicating the smallest change in geometry occurs when the bipyridyl binding group is used. However, a change in coordination number may also occur with this system by association of an acetonitrile ligand to give a calcu-

Table 1 Calculated λ values using PBE1PBE and B3PW91 methods for $[Cu(\mathbf{1})]^{2+/1+}$, $[Cu(\mathbf{1})(MeCN)]^{2+/1+}$, $[Cu(\mathbf{2})]^{2+/1+}$, $[Cu(\mathbf{3})]^{2+/1+}$, $[Cu(bpye)_2]^{2+/1+}$, and $[Cu(dmby)_2]^{2+/1+}$

Entry	Complex	PBE1PBE	B3PW91
1	$[Cu(\mathbf{1})]^{2+/1+}$	0.34 eV	0.34 eV
2	$[Cu(\mathbf{1})(MeCN)]^{2+/1+}$	0.53 eV	—
3	$[Cu(\mathbf{2})]^{2+/1+}$	0.40 eV	0.40 eV
4	$[Cu(\mathbf{3})]^{2+/1+}$	0.38 eV	0.38 eV
5	$[Cu(bpye)_2]^{2+/1+}$	0.58 eV	0.59 eV
6	$[Cu(dmby)_2]^{2+/1+}$	0.34 eV	0.30 eV

lated upper bound of 0.53 eV for λ. The introduction of the triazole group led to a modest increase in reorganization energies for $[Cu(\mathbf{2})]^{2+/1+}$ and $[Cu(\mathbf{3})]^{2+/1+}$ with comparable values of 0.40 and 0.38 eV, respectively, using either DFT method. For a comparison to literature-reported Cu RSs, the λ values for $[Cu(bpye)_2]^{2+/1+}$ and $[Cu(dmby)_2]^{2+/1+}$ were found to be 0.58–0.59 eV and 0.34–0.30 eV, respectively, depending upon method selection (Table 1, entries 5 and 6). This indicates that the tetradentate biphenyl-based Cu RSs have lower λ values relative to some bidentate copper complexes such as $[Cu(bpye)_2]^{2+/1+}$ and are comparable to the λ values determined for $[Cu(dmby)_2]^{2+/1+}$. The latter system is known to be a geometrically constrained four-coordinate complex due to designed steric effects on the bidentate ligands that restrict the range of motion. In addition, the tetradentate biphenyl-based Cu RSs have a lower reorganization energy compared to the commonly used $[Co(bpy)_3]^{3+/2+}$ RS with a λ value reported at 0.61 eV, and thus can potentially operate with lower ΔG_{reg} driving forces in DSC devices.[22]

While the crystallographic and computational values are not required to be in exact agreement due to different conditions (crystal packing interactions *versus* in isolation employing a solvent model), the values are in reasonable agreement between the two analyses for $[Cu(\mathbf{1})]^{1+}$ with a less than 6° variation between bond angles (Table 2, entry 1). A similar level of agreement was found between the computed and experimental values for $[Cu(\mathbf{1})(MeCN)]^{2+}$ (Table 2, entry 5). Upon oxidation of $[Cu(\mathbf{1})]^{1+}$ to $[Cu(\mathbf{1})]^{2+}$ or reduction of $[Cu(\mathbf{1})(MeCN)]^{2+}$ to $[Cu(\mathbf{1})(MeCN)]^{1+}$, the calculated bond angles shift by as much as 12° between the redox partners (Table 2, entries 3 and 6, respectively). Interestingly, the calculated structure of $[Cu(\mathbf{1})(MeCN)]^{1+}$ shows dissociation of a pyridine donor, where this Cu–N distance is 2.60 Å (Fig. S1†). The remaining nitrogen donors are bound in a distorted tetrahedral geometry about the Cu(I) metal center with an average Cu–N bond distance of 2.12 Å.

Reorganization energies were calculated for both redox couples where it was assumed the coordination sphere would remain 4-coordinate or 5-coordinate during the instant of electron transfer. Inner-sphere λ values are 0.34 eV for the 4-coordinate $[Cu(\mathbf{1})]^{2+/1+}$ redox pair and 0.53 eV for the 5-coordinate $[Cu(\mathbf{1})(MeCN)]^{2+/1+}$ redox pair. These values provide a lower and upper estimate for the internal reorganization energy for this system. For simplicity, the redox shuttle supported by tetradentate ligand **1** will generally be referred to as $[Cu(\mathbf{1})]^{2+/1+}$ unless otherwise specified. While the solid-state structures do not necessarily reflect the reactants and products of electron transfer in solution, the observation of a 5-coordinate Cu(II) species may explain the poor performance of $[Cu(\mathbf{1})]^{2+/1+}$ in DSC devices as described below.

Similar analysis was carried out for the $[Cu(\mathbf{2})]^{2+/1+}$ system comparing computational and experimental results (Table 2, entries 7–9), where reasonable agreement between theory and experiment was obtained. Similar changes are observed for $[Cu(\mathbf{3})]^{2+/1+}$ when compared with $[Cu(\mathbf{2})]^{2+/1+}$ (Table 2, entries 10–12). The benchmark RS $[Cu(bpye)_2]^{2+/1+}$ has bond angle changes of up to 38° upon oxidation state change, which is again consistent with the larger inner-sphere reorganization

Table 2 Computed bond angles at Cu for $[Cu(\mathbf{1})]^{2+/1+}$, $[Cu(\mathbf{1})(MeCN)]^{2+/1+}$, $[Cu(\mathbf{2})]^{2+/1+}$, $[Cu(\mathbf{3})]^{2+/1+}$, and $[Cu(bpye)_2]^{2+/1+}$ at the PBE1PBE level[a]

Entry	Complex	N1–Cu–N2	N1–Cu–N3	N1–Cu–N4	N2–Cu–N3
1	$[Cu(\mathbf{1})]^{1+}$	79.533 (81.5)	129.845 (135.4)	112.033 (108.1)	131.512 (128.4)
2	$[Cu(\mathbf{1})]^{2+}$	81.863	140.420	99.901	121.460
3	$\Delta[Cu(\mathbf{1})]^{2+/1+}$	2.33	10.575	12.132	10.052
4	$[Cu(\mathbf{1})(MeCN)]^{1+}$	76.304	122.624	90.626	126.348
5	$[Cu(\mathbf{1})(MeCN)]^{2+}$	80.529 (81.04)	111.126 (106.65)	94.043 (93.12)	119.243 (115.59)
6	$\Delta[Cu(\mathbf{1})(MeCN]^{2+/1+}$	4.225	11.498	3.417	7.105
7	$[Cu(\mathbf{2})]^{1+}$	79.966 (80.7)	142.578 (145.9)	118.844 (110.7)	104.918 (108.6)
8	$[Cu(\mathbf{2})]^{2+}$	82.096 (82.0)	152.761 (154.0)	103.812 (103.7)	104.949 (104.1)
9	$\Delta[Cu(\mathbf{2})]^{2+/1+}$	2.13 (1.3)	10.183 (8.1)	15.032 (7.0)	0.031 (4.5)
10	$[Cu(\mathbf{3})]^{1+}$	79.974	142.694	118.065	105.724
11	$[Cu(\mathbf{3})]^{2+}$	82.035	152.447	103.743	105.435
12	$\Delta[Cu(\mathbf{3})]^{2+/1+}$	2.061	9.753	14.322	0.289
13	$[Cu(bpye)_2]^{1+}$	92.285	116.676	112.856	
14	$[Cu(bpye)_2]^{2+}$	88.426	154.780	98.580	
15	$\Delta[Cu(bpye)_2]^{2+/1+}$	3.859	38.104	14.276	

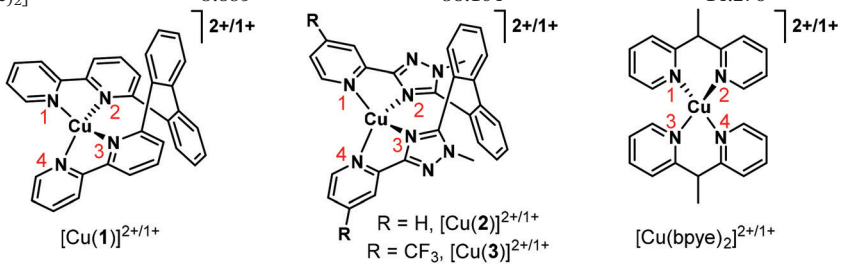

[a] Values in parentheses are from reported crystal structures.[39,42] The term Δ in entries 3, 6, 9, 12, and 15 refers to the change in bond angle between the two oxidation states. The angles measured are coded in red numbers on the structures.

energy observed for this RS (Table 2, entries 13–15). These results confirm that the strategy of restricting the Cu RS geometry with a rigid polyaromatic tetradentate ligand has successfully reduced geometric changes and, in turn, lowered internal reorganization energies.

Optical measurements were conducted on the tetradentate RSs *via* absorption spectroscopy to ensure the Cu RSs do not block light transmission into the DSC devices. Cyclic voltammetry was used to assess the reversibility of the Cu(II/I) redox couples and the thermodynamic suitability of these RSs for use with benchmark dye **Y123** (Fig. 4 and Table 3). Cu RSs $[Cu(\mathbf{1})]^{1+}$ and $[Cu(\mathbf{2})]^{1+}$ both have significant high energy absorption bands with peaks ranging from 442–465 nm and molar absorptivities of 4400–1300 M^{-1} cm^{-1}. The onset of these absorption bands range from 550–650 nm. The absorption bands cover a significant cross section of the visible region, which can block light from photoexciting dye molecules and thus lower device efficiencies. However, the molar absorptivity values are low compared to $[Cu(dmby)_2]^{1+}$ which is known to operate at a high efficiency in DSC devices despite an ε value of 6900 M^{-1} cm^{-1} in the visible region at 455 nm with the band extending out to 590 nm.[22] This indicates that competitive absorbance of $[Cu(\mathbf{1})]^{1+}$ and $[Cu(\mathbf{2})]^{1+}$ is not strong enough to dramatically inhibit device performances. The $[Cu(\mathbf{1})]^{2+}$, $[Cu(\mathbf{2})]^{2+}$, and $[Cu(\mathbf{3})]^{2+}$ complexes all show d–d transitions as the lowest energy feature in the absorption spectrum, ranging from 764–780 nm with onsets from 900–1100 nm. As expected for metal-based d–d transitions, the molar absorptivities of these bands are low and range from 73–292 M^{-1} cm^{-1}. These values are comparable to those observed for both benchmark Cu RSs, $[Cu(bpye)_2]^{2+}$ and $[Cu(dmby)_2]^{2+}$.[21,22] The higher energy absorption bands for $[Cu(\mathbf{1})]^{2+}$ and $[Cu(\mathbf{2})]^{2+}$ in the visible region are weakly absorbing (ε of 400 and 55 M^{-1} cm^{-1}, respectively); however, $[Cu(\mathbf{3})]^{2+}$ absorbs more strongly in this region with a molar absorptivity of 1950 M^{-1} cm^{-1} for a band positioned at 347 nm and extending out to 440 nm (Fig. S2†). While this molar extinction coefficient is higher for $[Cu(\mathbf{3})]^{2+}$ relative to the other biphenyl-based Cu RSs, this absorption band is at higher energy and comparable to the high performing benchmark shuttle $[Cu(dmby)_2]^{2+}$.[22] Based on these observations, $[Cu(\mathbf{1})]^{2+}$, $[Cu(\mathbf{2})]^{2+}$, and $[Cu(\mathbf{3})]^{2+}$ have the potential to function well in DSC devices with only a modest loss in efficiency due to competitive light absorption in the visible region of the solar spectrum.

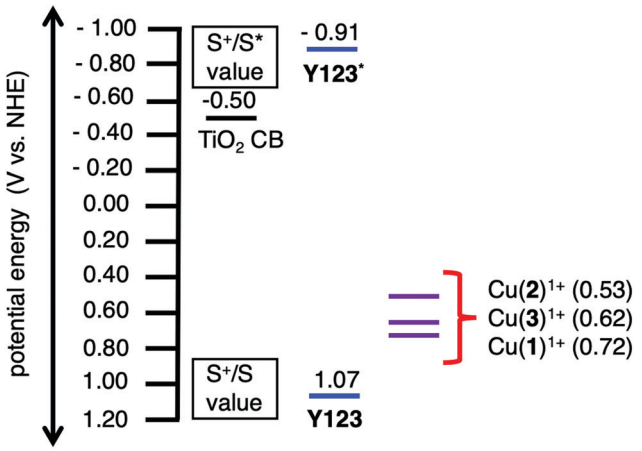

Fig. 4 Energy level diagram for **Y123**, $[Cu(\mathbf{1})]^{2+/1+}$, $[Cu(\mathbf{2})]^{2+/1+}$, and $[Cu(\mathbf{3})]^{2+/1+}$. The TiO_2 conduction band (CB) is taken as −0.50 V *vs.* NHE in MeCN as is generally approximated in the field.[59–61]

Cyclic voltammetry studies show that the redox shuttles have potentials ranging from 0.53–0.72 V *versus* NHE with the following order: $[Cu(\mathbf{2})]^{2+/1+}$ < $[Cu(\mathbf{3})]^{2+/1+}$ < $[Cu(\mathbf{1})]^{2+/1+}$ (Table 3, Fig. S3†). Each of the redox shuttles are energetically positioned for a favorable electron transfer to $[\mathbf{Y123}]^{+}$ (**Y123** oxidation potential of 1.07 V)[22] with ΔG_{reg} values ranging from 350–540 mV. We note that the pK_a of pyridine is 5.2 and for 1-methyl-1,2,4-triazole, the pK_a is 3.2, which suggests that pyridine is the more basic donor.[56] The more positive potential of the $[Cu(\mathbf{1})]^{2+/1+}$ couple is presumably due to the significantly different geometry engendered by four 6-membered pyridine donors *versus* replacing two of these heterocycles with 5-membered 1,2,4-triazole groups. Kubiak and coworkers have recently introduced a new geometric index, τ_δ, to classify complexes with 4-coordinate geometries within the limiting extremes of square planar (τ_δ = 0) and tetrahedral (τ_δ = 1).[57]

Table 3 Optical and electrochemical properties of Cu redox shuttles

Entry	Complex	λ_{high} (nm)	λ_{high}^{onset} (nm)	ε_{high} (M^{-1} cm^{-1})	λ_{d-d} (nm)	λ_{d-d}^{onset} (nm)	ε_{d-d} (M^{-1} cm^{-1})	$Cu^{2+/1+}$ (V *vs.* NHE)	ΔE_p [a] (mV)
1	$[Cu(\mathbf{1})]^{1+}$	465	650	4400	—	—	—	0.72	100
2[b,c]	$[Cu(\mathbf{1})]^{2+}$	400	—	400	764	—	180	—	—
3[d]	$[Cu(\mathbf{2})]^{1+}$	442	550	1300	—	—	—	0.53	132
4[d]	$[Cu(\mathbf{2})]^{2+}$	344	440	55	799	>900	73	—	—
5	$[Cu(\mathbf{3})]^{1+}$	—	—	—	—	—	—	0.62	260
6	$[Cu(\mathbf{3})]^{2+}$	347	440	1950	780	1100	292	—	—
7[e]	$[Cu(bpye)_2]^{1+}$	~425 (sh)	480	350	—	—	—	0.59	900
8[e]	$[Cu(bpye)_2]^{2+}$	—	—	—	~560	700	50	—	—
9[f]	$[Cu(dmby)_2]^{1+}$	455	590	6900	—	—	—	0.97	~80
10[f]	$[Cu(dmby)_2]^{2+}$	360	500	1300	~725	>900	~390	—	—

[a] $\Delta E_p = E_{p,c} - E_{p,a}$ where $E_{p,c}$ is the cathodic peak potential and $E_{p,a}$ is the anodic peak potential. [b] Reported values from ref. 39. [c] Data reported in the presence of chloride ions. [d] Reported values from ref. 42. [e] Reported values from ref. 21. [f] Reported values from ref. 22.

From the crystal structures of $[Cu(\mathbf{1})]^{1+}$ and $[Cu(\mathbf{2})]^{1+}$, the τ_δ values are 0.65 and 0.50, respectively, indicating that $[Cu(\mathbf{1})]^{1+}$ is best described as having a distorted tetrahedral geometry while $[Cu(\mathbf{2})]^{1+}$ is best described as having a distorted sawhorse geometry. The tunability of the biphenyl-based redox shuttles following substitutions at the 4-position of the pyridine is apparent when $[Cu(\mathbf{3})]^{2+/1+}$ and $[Cu(\mathbf{2})]^{2+/1+}$ are compared. The CF_3 groups of $[Cu(\mathbf{3})]^{2+/1+}$ result in a 90 mV more positive redox potential. Notably, the peak-to-peak separations (ΔE_p) observed in CVs at a scan rate of 100 mV s^{-1} show that the $[Cu(\mathbf{3})]^{2+/1+}$ couple has a significantly larger peak splitting of 260 mV compared to $[Cu(\mathbf{1})]^{2+/1+}$ and $[Cu(\mathbf{2})]^{2+/1+}$ which have ΔE_p values of 100–132 mV. We note that a peak splitting of 59 mV is expected for an ideal, reversible one-electron process at standard temperature.[58] In comparison to the two benchmark systems, the ΔE_p values are larger than that of $[Cu(dmby)_2]^{2+/1+}$ at 80 mV, but dramatically less than that of $[Cu(bpye)_2]^{2+/1+}$ at 900 mV.[21,22] These results are again consistent with calculated reorganization energies where the same trend is observed with increasing ΔE_p values correlating with increasing inner-sphere λ values. A low reorganization energy and smaller ΔE_p values suggest that electron transfers will be rapid in DSC devices which may result in lower ΔG_{reg} values being needed and more efficient devices.

Notably, the relatively small ΔE_p value (100 mV) for the $[Cu(\mathbf{1})]^{2+/1+}$ couple suggests that there is not a change in coordination number between the two oxidation states on this timescale. In addition, the Cu(I) complex is the dominant component of the redox electrolyte, which is comprised of 0.2 M Cu(I) species and 0.04 M Cu(II) species. Dye regeneration is thus from the 4-coordinate $[Cu(\mathbf{1})]^{1+}$ complex, in which electron transfer is expected to occur through a 4-coordinate transition state. However, slow electron transfer kinetics at the counter electrode may result if formation of the 5-coordination Cu(II) species $[Cu(\mathbf{1})(MeCN)]^{2+}$ occurs.

DSC devices were fabricated with $[Cu(\mathbf{1})]^{2+/1+}$, $[Cu(\mathbf{2})]^{2+/1+}$, $[Cu(\mathbf{3})]^{2+/1+}$, $[Cu(bpye)_2]^{2+/1+}$, and $[Co(bpy)_3]^{3+/2+}$ as the RSs with organic dye **Y123** common to each device. **Y123** has been studied thoroughly in the literature and is one of the best performing dyes in terms of limiting detrimental recombination of electrons in the TiO_2 conduction band with the oxidized redox shuttle.[22,24,62–69] Energetically **Y123** is well matched with these Cu RSs as described above (Fig. 4), and this dye provides direct literature comparisons to $[Co(bpy)_3]^{3+/2+}$ and $[Cu(bpye)_2]^{2+/1+}$ based devices to benchmark the Cu-shuttle device performance metrics. Current–voltage (J–V) curves were collected for each DSC device, and power conversion efficiencies (PCEs) were calculated according to the equation: PCE = $(J_{SC} \times V_{OC} \times FF)/I_0$, where J_{SC} is the short-circuit current density, V_{OC} is the open-circuit voltage, FF is the fill factor, and I_0 is the incident light intensity set to 1 sun for this study (Fig. 5 and S4,† Table 4). Devices based on $[Cu(\mathbf{1})]^{2+/1+}$ with PEDOT counter electrodes show a low J_{SC} value of 5.7 mA cm^{-2} relative to the two benchmark systems using $[Cu(bpye)_2]^{2+/1+}$

Table 4 DSC device performance parameters

Entry	Redox shuttle	Counter electrode	V_{OC} (mV)	J_{SC} (mA cm^{-2})	FF	PCE (%)
1	$[Cu(\mathbf{1})]^{2+/1+}$	PEDOT	689	5.7	0.77	3.1
2	$[Cu(\mathbf{2})]^{2+/1+}$	Pt	641	14.1	0.45	4.1
3		PEDOT	693	10.2	0.72	4.7
4	$[Cu(\mathbf{3})]^{2+/1+}$	Pt	678	10.2	0.45	3.2
5		PEDOT	792	7.9	0.75	4.3
6	$[Co(bpy)_3]^{3+/2+}$	Pt	864	14.2	0.67	8.1
7		PEDOT	818	14.6	0.73	8.9
8	$[Cu(bpye)_2]^{2+/1+}$	Pt	651	9.7	0.48	3.1
9		PEDOT	627	13.2	0.65	5.6

Values are the average of at least two devices, and PCE values vary by no more than ±0.4%. Standard conditions: TiO_2 films were prepared with a 5.0 μm TiO_2 (28–30 μm nanoparticles) film under a 4.5 μm TiO_2 (>100 μm nanoparticle size) scattering layer film. The TiO_2 film is sensitized with a 0.2 mM (1 : 1 CH_3CN : tBuOH) **Y123** solution for 16 hours. Electrolyte composition: 0.20 M Cu^{1+}, 0.04 M Cu^{2+}, 0.1 M lithium bis(trifluoromethane)sulfonimide (LiTFSI), and 0.5 M 4-*tert*butylpyridine (TBP) in MeCN.

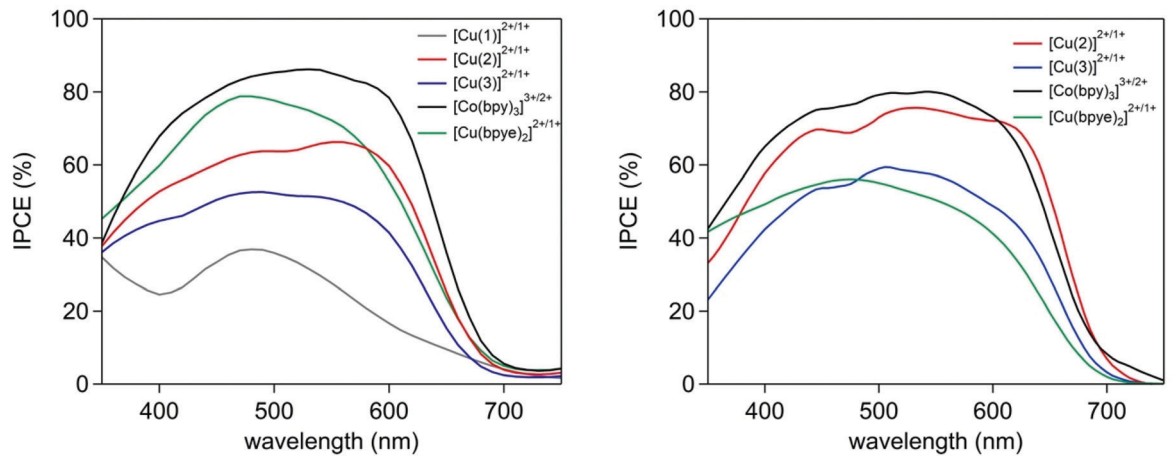

Fig. 5 IPCE curves of DSC devices fabricated with PEDOT counter electrodes (left) or Pt counter electrodes (right) using Cu and Co RSs as specified with dye **Y123**.

(J_{SC} = 13.2 mA cm^{-2}) and $[Co(bpy)_3]^{3+/2+}$ (J_{SC} = 14.8 mA cm^{-2}) prepared in our laboratory under identical conditions using a PEDOT (poly(3,4-ethylenedioxythiophene)) counter electrode as is commonly used in transition metal based DSC devices due to a low charge transfer resistance relative to other commonly used materials such as platinum.[70] Accordingly, the corresponding incident photon-to-current conversion efficiency (IPCE) graph shows a peak IPCE value of 37% for $[Cu(\mathbf{1})]^{2+/1+}$ with values near 80% for $[Cu(bpye)_2]^{2+/1+}$ and $[Co(bpy)_3]^{3+/2+}$ (Fig. 5). The origin of this low J_{SC} value is likely related to the poor stability of $[Cu(\mathbf{1})]^{2+/1+}$ in DSC devices as device performance was observed to drop even under low indoor lighting exposure with the overall η values rapidly deteriorating from 3.1% at time zero to 1.7% after 24 hours of ambient light exposure (Fig. 6). A pathway to decomposition of this RS may result from the accessibility of a 5-coordinate Cu(II) species (Fig. 3) and dissociation of a pyridine from the tetradentate ligand following reduction to $[Cu(\mathbf{1})(MeCN)]^{1+}$, as predicted by the calculated structure shown in Fig. S1.† Given the low stability of this redox shuttle, no further device characterization was pursued.

Importantly, upon changing two of the pyridyl groups of $[Cu(\mathbf{1})]^{2+/1+}$ to two 4-methyl-1,2,4-triazole groups to give $[Cu(\mathbf{2})]^{2+/1+}$, the J_{SC} value improved to 10.2 mA cm^{-2} using PEDOT counter electrodes. Although J_{SC} was improved, the devices were not stable losing 27% of the J_{SC} value over 24 hours to 7.4 mA cm^{-2} (Table 5). To further evaluate the performance of $[Cu(\mathbf{2})]^{2+/1+}$, DSC devices with Pt counter electrodes were fabricated. Surprisingly, these devices were able to generate J_{SC} values as high as 14.1 mA cm^{-2} which is nearly equivalent to $[Co(bpy)_3]^{3+/2+}$ and higher than that observed with $[Cu(bpye)_2]^{2+/1+}$ under identical conditions (Table 4). The IPCE peak value for $[Cu(\mathbf{2})]^{2+/1+}$-Pt is similar to that of $[Co(bpy)_3]^{3+/2+}$-Pt at near 80% (Fig. 5). The $[Cu(\mathbf{2})]^{2+/1+}$, $[Cu(bpye)_2]^{2+/1+}$, and $[Co(bpy)_3]^{3+/2+}$ redox potentials are closely grouped between 0.53–0.59 V *vs.* NHE which allows for a comparison of V_{OC} values. Under these conditions, the V_{OC} trend for the Pt devices is in the following order from highest to lowest: $[Co(bpy)_3]^{3+/2+} \gg [Cu(bpye)_2]^{2+/1+} > [Cu(\mathbf{2})]^{2+/1+}$. DSC devices based on $[Cu(\mathbf{3})]^{2+/1+}$ gave the highest V_{OC} value among the Cu RSs with Pt counter electrodes at 678 mV and at 792 mV for devices fabricated with PEDOT counter electrodes (Table 4). These results were expected as the redox potential of $[Cu(\mathbf{3})]^{2+/1+}$ is the most positive of the series by 30 mV leading to a higher possible maximum voltage; however, the photocurrent decreased to 10.2 mA cm^{-2} for Pt based devices and 7.9 mA cm^{-2} for PEDOT based devices with a representative decrease in the peak IPCE value leading to an overall lower device efficiency compared to $[Cu(\mathbf{2})]^{2+/1+}$ (3.2% *versus* 4.1%, respectively, for Pt based devices; and 4.3% *versus* 4.7% for PEDOT based devices).

In the absence of a conduction band (CB) shift, the lost V_{OC} (V_{OC}^{loss}) due to non-productive electron transfer pathways can be described according to the equation $V_{OC}^{loss} = V_{OC}^{max} - V_{OC}^{obs}$, where V_{OC}^{max} is the maximum V_{OC} possible (taken as the difference in energy between the TiO_2 CB at −0.5 V *vs.* NHE[2] and the redox potential of the redox shuttle) and V_{OC}^{obs} is the observed V_{OC} from the DSC devices. In this case, the trend for V_{OC}^{loss} for devices made with Pt counter electrodes from least to greatest losses is: $[Cu(\mathbf{2})]^{2+/1+} < [Cu(bpye)_2]^{2+/1+} < [Cu(\mathbf{3})]^{2+/1+}$ and ranges from 390 mV to 440 mV. Interestingly, the FF values for the Pt based devices were significantly lower for all Cu RSs relative to

Table 5 DSC device stability data for $[Cu(\mathbf{1})]^{2+/1+}$-PEDOT, $[Cu(\mathbf{2})]^{2+/1+}$-Pt, and $[Cu(\mathbf{2})]^{2+/1+}$-PEDOT

Entry	Redox shuttle	Counter electrode	Time (hours)	V_{OC} (mV)	J_{SC} (mA cm^{-2})	FF	PCE (%)
1	$[Cu(\mathbf{1})]^{2+/1+}$	PEDOT	0	689	5.7	0.77	3.1
2			24	618	4.2	0.67	1.8
3			48	605	2.9	0.74	1.4
4			336	470	0.5	0.62	0.2
5	$[Cu(\mathbf{2})]^{2+/1+}$	Pt	0	641	14.1	0.45	4.1
6			1	671	13.0	0.49	4.4
7			24	630	12.5	0.42	3.2
8			48	686	12.3	0.47	3.9
9			72	643	8.1	0.60	3.1
10	$[Cu(\mathbf{2})]^{2+/1+}$	PEDOT	0	693	10.2	0.72	4.7
11			1	712	10.7	0.68	4.8
12			24	784	7.4	0.76	4.5

Values are the average of at least two devices, and PCE values vary by no more than ±0.4%. Standard conditions: TiO_2 films were prepared with a 5.0 μm TiO_2 (28–30 μm nanoparticles) film under a 4.5 μm TiO_2 (>100 μm nanoparticle size) scattering layer film. The TiO_2 film is sensitized with a 0.2 mM (1 : 1 MeCN : *t*BuOH) **Y123** solution for 16 hours. Electrolyte composition: 0.20 M Cu^{1+}, 0.04 M Cu^{2+}, 0.1 M LiTFSI, and 0.5 M TBP in MeCN.

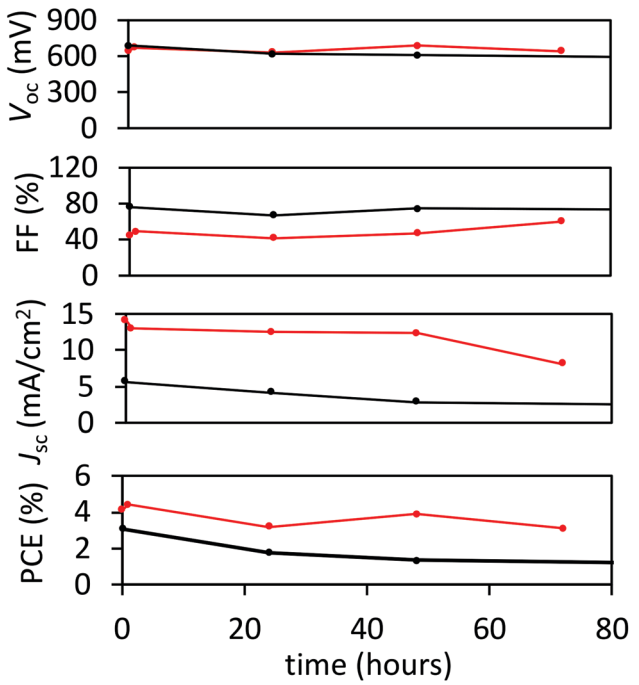

Fig. 6 Stability curves for $[Cu(\mathbf{1})]^{2+/1+}$-PEDOT (black lines) and $[Cu(\mathbf{2})]^{2+/1+}$-Pt (red lines).

$[Co(bpy)_3]^{3+/2+}$ (0.45–0.48 *versus* 0.67) although the origin of these lower values is not obvious. Notably, attempts to make solid state cells using the biphenyl-based Cu RSs by either initial evaporation of solvent in a glove box or by continuous illumination of the cells resulted in non-functional devices indicating that these shuttles do not function as solid-state hole transport materials under the conditions tested.

To understand the V_{OC} trends, electrochemical impedance spectroscopy (EIS) and small modulated photovoltage transient (SMPVT) measurements were undertaken with $[Cu(\mathbf{2})]^{2+/1+}$ and $[Cu(\mathbf{3})]^{2+/1+}$ (Fig. 7, 8, S5† and Tables 6 and S1†). The EIS Nyquist plot was fitted using a typical circuit (Fig. S6†) with the first smaller semi-circle relating to the redox shuttle charge transfer resistance at the counter electrode and the larger semi-circle relating to the charge transfer resistance at the TiO_2–dye/electrolyte interface (Fig. 7, Table 6). Charge transfer resistance at the platinum counter electrode (R_{CE}) was significantly higher for $[Cu(bpye)_2]^{2+/1+}$ (92 Ω) when compared with $[Cu(\mathbf{2})]^{2+/1+}$ and $[Cu(\mathbf{3})]^{2+/1+}$ (43 and 25 Ω). The trend in resistance at the counter electrode is as follows: $[Cu(bpye)_2]^{2+/1+} \gg [Cu(\mathbf{2})]^{2+/1+} > [Co(bpy)_3]^{3+/2+} > [Cu(\mathbf{3})]^{2+/1+}$. When examining charge transfer resistances at the TiO_2–dye/electrolyte interface (R_{REC}), a significantly lower charge transfer resistance is observed for the $[Cu(\mathbf{2})]^{2+/1+}$ and $[Cu(\mathbf{3})]^{2+/1+}$ shuttles relative to $[Co(bpy)_3]^{3+/2+}$ and $[Cu(bpye)_2]^{2+/1+}$ (~100 Ω *versus* ~200 Ω). Given that $[Co(bpy)_3]^{3+/2+}$ is known to have a significantly faster recombination (lower charge transfer resistance *via* EIS) of electrons in the TiO_2 CB with the oxidized redox shuttle relative to the traditional I^-/I_3^- RS system, the $[Cu(\mathbf{2})]^{2+}$ and $[Cu(\mathbf{3})]^{2+}$ shuttles likely have exceptionally facile TiO_2 CB electron recombination kinetics given the dramatically lower charge transfer resistance at the TiO_2–dye/electrolyte interface. The charge collection efficiency (η_{cc}) for the productive electron transfer pathway can be found through the equation $\eta_{cc} = 1/(1 + (R_{CE}/R_{REC}))$. The highest charge collection efficiency is observed with $[Co(bpy)_3]^{3+/2+}$ at 87%. Both $[Cu(\mathbf{2})]^{2+/1+}$ and $[Cu(\mathbf{3})]^{2+/1+}$ have relatively smaller η_{cc} values at 72% and 79%, respectively, due to the smaller R_{REC} values relative to the Co RS. The lowest η_{cc} were observed with $[Cu(bpye)_2]^{2+/1+}$ with a Pt counter electrode at 67% due to a high R_{CE}. When these values are compared to the peak IPCE values (Fig. 5), $[Cu(\mathbf{2})]^{2+/1+}$ is observed to have negligible remaining loss pathways with a similar peak IPCE value to the observed η_{cc} value. The remaining RSs show a significantly lower peak IPCE (~10% lower)

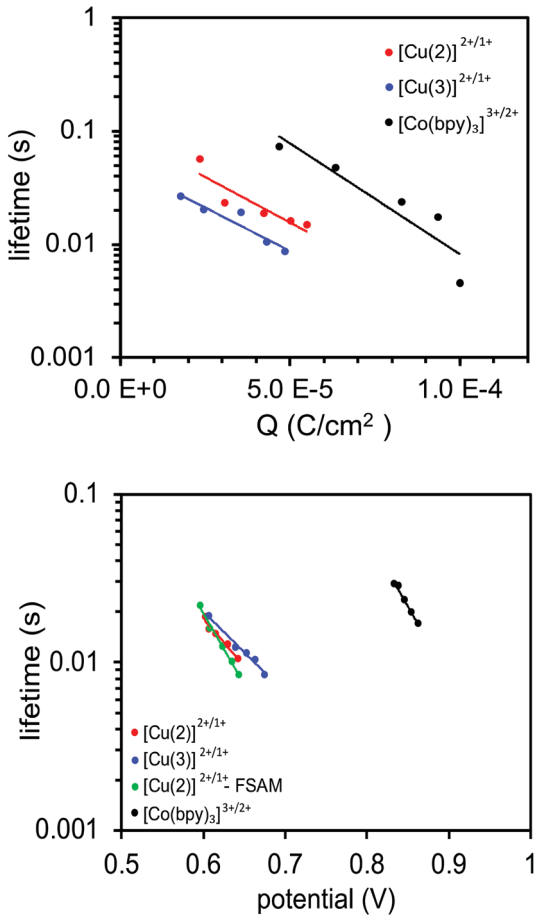

Fig. 8 A plot of electron lifetime *versus* capacitance (top) and a plot of electron lifetime *versus* open-circuit voltage from SMPVT (bottom) with DSC devices based on Cu and Co RSs with Pt electrodes.

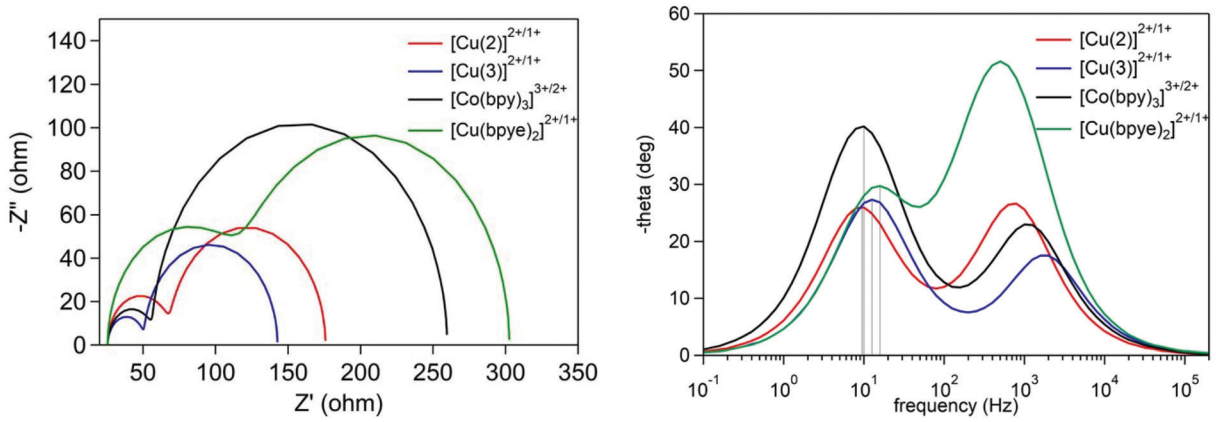

Fig. 7 Nyquist (left) and Bode (right) plots of DSC devices with Cu and Co RSs with platinum counter electrodes.

Table 6 EIS data from $[Cu(\mathbf{2})]^{2+/1+}$, $[Cu(\mathbf{3})]^{2+/1+}$, $[Co(bpy)_3]^{3+/2+}$, and $[Cu(bpye)_2]^{2+/1+}$ based DSC devices with Pt as the counter electrode

Entry	Redox shuttle	R_S (Ω)	R_{REC} (Ω)	C_μ (mF)	R_{CE} (Ω)	C_{CE} (mF)	η_{cc} (%)	τ_{TiO_2} (ms)
1	$[Cu(\mathbf{2})]^{2+/1+}$	28	108	2.7×10^{-4}	43	7.9×10^{-6}	72	15.9
2	$[Cu(\mathbf{3})]^{2+/1+}$	30	92	2.2×10^{-4}	25	4.8×10^{-6}	79	12.6
3	$[Co(bpy)_3]^{3+/2+}$	26	203	1.8×10^{-4}	31	6.8×10^{-6}	87	15.9
4	$[Cu(bpye)_2]^{2+/1+}$	15	185	1.1×10^{-1}	92	9.0×10^{-4}	67	10.0

R_s is the series resistance, R_{rec} is the recombination resistance of electrons in TiO_2 across the TiO_2–dye interface to an oxidized redox shuttle, C_μ is the chemical capacitance for charge accumulation in TiO_2, R_{CE} is the electron-transfer resistance at the counter electrode to an oxidized redox shuttle, and C_{CE} is the capacitance at the electrolyte-counter electrode interface. $\tau_{TiO_2} = 1/(2\pi f)$, where τ_{TiO_2} is the lifetime of injected electrons in TiO_2 and f is the peak frequency from the Bode plot for the lower frequency peak between 10 and 100 Hz (shown as gray lines in Fig. 7).

relative to the observed η_{cc} values, which indicates additional loss mechanisms are likely operative.

Bode plot analysis of the EIS measurements allows for the observation of electron lifetime in TiO_2 (τ_{TiO_2}), at the lower frequency peak (marked with gray lines in Fig. 7) where electron transfer from the TiO_2–dye interface to the electrolyte is observed. From the equation $\tau_{TiO_2} = 1/(2\pi f)$, electron lifetimes can be calculated which show the following order $[Cu(\mathbf{2})]^{2+/1+} = [Co(bpy)_3]^{3+/2+} > [Cu(\mathbf{3})]^{2+/1+} > [Cu(bpye)_2]^{2+/1+}$. These values are not directly correlated with the V_{OC}^{loss} values which suggests recombination may not be the only factor affecting the V_{OC}^{loss} values.[71,72] These measurements are in contrast to those observed with a capacitance *versus* lifetime plot (Fig. 8) which is a second method of assessing recombination losses through a photoinitiated process that may be more directly related to the actual solar cell environment in the functional devices in this case.

Charge extraction measurements were conducted and plotted as electron lifetime *versus* capacitance (Q) for DSC devices with Pt counter electrodes (Fig. 8). A longer electron lifetime is obtained at the same Q value in the presence of $[Cu(\mathbf{2})]^{2+/1+}$ when compared with $[Cu(\mathbf{3})]^{2+/1+}$. This indicates that in the presence of $[Cu(\mathbf{2})]^{2+/1+}$ there are fewer recombination events, which leads to a higher device performance with this redox shuttle when compared to $[Cu(\mathbf{3})]^{2+/1+}$. Both lifetimes at constant Q are shorter for the Cu-RSs than for the $[Co(bpy)_3]^{3+/2+}$ benchmark RS. Directly relating V_{OC} values to any one parameter is challenging since many factors affect photovoltage including: (1) differences in RS oxidation potentials leading to different V_{OC}^{max} values for each RS, (2) varied capacitance between devices, (3) differences in recombination rates, and (4) conduction band shifts that can occur.[73,74] A V_{OC} *versus* lifetime plot allows for a summing of all of the voltage loss (V_{OC}^{loss}) events with a correlation to electron lifetime when accounting for the redox potential of each RS. A linear relationship between electron lifetime and voltage is observed *via* small modulated photovoltage transient (SMPVT) spectroscopy (Fig. 8). From the SMPVT data, a smaller V_{OC}^{loss} value and longer lifetime is observed for $[Co(bpy)_3]^{3+/2+}$ (0.20 V_{OC}^{loss}) relative to the remaining redox shuttles (0.39–0.44 V_{OC}^{loss}). The close grouping of electron lifetimes for the Cu-RSs agrees well with the close V_{OC}^{loss} values observed. A reasonable explanation for similar electron lifetime (and V_{OC}^{loss}) values for $[Cu(\mathbf{2})]^{2+/1+}$, $[Cu(\mathbf{3})]^{2+/1+}$, and $[Cu(bpye)_2]^{2+/1+}$ is that the smaller λ value (~200 mV smaller) for $[Cu(\mathbf{2})]^{2+/1+}$ and $[Cu(\mathbf{3})]^{2+/1+}$ allows for faster charge extraction from the counter electrode than $[Cu(bpye)_2]^{2+/1+}$ (see EIS section above). However, the larger charge transfer resistance of $[Cu(bpye)_2]^{2+/1+}$ at the TiO_2–dye interface slows non-productive electron transfers (decreased V_{OC}^{loss}) to yield a similar V_{OC}^{loss} for the Cu-RSs.

Conclusions

Three tetradentate ligated Cu redox shuttles ($[Cu(\mathbf{1})]^{2+/1+}$, $[Cu(\mathbf{2})]^{2+/1+}$, and $[Cu(\mathbf{3})]^{2+/1+}$) were targeted and evaluated computationally, electrochemically, and in DSC devices using a benchmark organic dye, **Y123**. The quantum chemically computed inner-sphere λ values for the biphenyl-based Cu RSs were relatively low at 0.34–0.53 eV. Compared to the well-established $[Co(bpy)_3]^{3+/2+}$ RS with a λ value reported at 0.61 eV, the Cu RSs reported here have a lower reorganization energy and thus can potentially operate with lower ΔG_{reg} driving forces in DSC devices. Interestingly, $[Cu(\mathbf{2})]^{2+/1+}$-Pt was found to give J_{SC} values (14.1 mA cm^{-2}) comparable to $[Co(bpy)_3]^{3+/2+}$-Pt (14.2 mA cm^{-2}) and higher than $[Cu(bpye)_2]^{2+/1+}$-Pt (9.7 mA cm^{-2}). The stability of the DSC devices for $[Cu(\mathbf{2})]^{2+/1+}$-Pt was observed to be higher when compared to $[Cu(\mathbf{2})]^{2+/1+}$-PEDOT. Evidence of high current and low inner-sphere reorganization energies with $[Cu(\mathbf{2})]^{2+/1+}$ in DSC devices, despite the observed drawback of a lower than usual fill factor (FF), warrants further exploration. The rigid tetradentate ligand design reduces structural changes associated with redox cycling, leading to an improved J_{SC} value and higher stability for $[Cu(\mathbf{2})]^{2+/1+}$-Pt based devices. Structurally constrained, preorganized ligands must be suitably matched to the metal ion to obtain sufficiently strong metal–ligand bonding interactions, in addition to the desired coordination geometry. Based on the low stability and poor performance of $[Cu(\mathbf{1})]^{2+/1+}$, it is apparent that changes to the coordination number of the redox shuttle by solvent binding and/or ligand dissociation should be avoided. The synthesis of next-generation copper redox shuttles featuring tunable tetradentate ligands is underway in our group in order to increase the FF while maintaining the high J_{SC} values and low inner-sphere electron transfer reorganization energies.

Experimental section

Unless otherwise noted, all reactions were carried out under inert atmosphere using standard Schlenk techniques. Compounds diphenic acyl chloride,[42] 2,2′-di([2,2′-bipyridin]-6-yl)-1,10-biphenyl,[46] and sets of copper complexes $[Cu(\mathbf{1})]^{2+}$ and $[Cu(\mathbf{1})]^{1+}$ as well as $[Cu(\mathbf{2})]^{2+}$ and $[Cu(\mathbf{2})]^{1+}$ have been reported in the literature.[39,42] The complexation of $[Cu(\mathbf{1})]^{2+/1+}$ and $[Cu(\mathbf{2})]^{2+/1+}$ redox shuttles was performed as described below for $[Cu(\mathbf{3})]^{2+}$ and $[Cu(\mathbf{3})]^{1+}$.

4-Trifluoromethyl-2-amidrazone pyridine (2)

1.75 g (10 mmol) of 4-trifluoromethyl-2-cyanopyridine (**1**) was dissolved in 5 mL of absolute ethanol. 1.05 mL (20 mmol) of methylhydrazine was added to the alcohol solution and stirred for 3 days. The intermediate was isolated by removal of solvent at room temperature and washing with hexanes resulting in the amidrazone intermediate as a fine brown powder (isolated yields were variable from ~30–55%). The amidrazone intermediate is temperature sensitive and should be stored in a freezer. ^{1}H NMR (500 MHz, $CDCl_3$) δ 8.65 (d, 1H), 8.32 (s, 1H), 7.43 (d, 1H), 5.15 (d, 2H), 3.01 (s, 3H). ^{13}C NMR (126 MHz, $CDCl_3$) δ 38.72, 115.82, 118.67, 119.57, 121.74, 123.91, 126.08, 138.15, 138.42, 138.69, 138.97, 144.88, 148.82, 152.27.

2,2′-Bis(methyltriazole-4-trifluoromethylpyridine)-biphenyl (3)

The synthesis was adapted from a similar procedure. Diphenic acyl chloride[42] (0.275 g, 1 mmol) was dissolved into 10 mL of THF. In a separate flask, **2** (0.436 g, 2 mmol) was dissolved into a 25 mL solution of THF. Triethylamine (0.253 g, 2.5 mmol) was added to the amidrazone solution and vigorously stirred at 0 °C for 10 minutes. While maintaining 0 °C, the diphenic acyl chloride solution was added dropwise resulting in an exothermic reaction and formation of a yellowish white suspension. The suspension was allowed to stir for an hour at 0 °C and isolated *via* frit funnel. The solid was washed with a mixture of methanol and water (1 : 1) three times. The resulting white precipitate was then heated to 250 °C until forming a brown clear melt. The oily melt was cooled to room temperature and dissolved into acetone. The solvent was removed under reduced pressure making foam-like powder. To ensure full cyclization of the amide intermediate, the foam was heated at 80 °C under reduced pressure until a tan crystalline powder appeared: quantitative yield. ^{1}H NMR (500 MHz, $CDCl_3$): δ 8.72 (d, 2H), 8.05 (s, 2H), 3.51 (s, 6H), 7.36 (dd, 2H), 7.39 (dd, 2H), 7.49 (dd, 2H), 7.53 (dd, 2H), 7.60 (dd, 2H). ^{13}C NMR (126 MHz, $CDCl_3$): δ 159.75, 155.15, 150.81, 150.62, 139.88, 139.19, 138.93, 138.67, 131.67, 131.26, 130.93, 128.31, 126.76, 123.77, 121.59, 119.39, 118.87, 116.98. HRMS: $[M + Cs]^+$ = $C_{30}H_{20}F_6N_8Cs$ calcd: 739.0770, found: 739.0742.

Synthesis of $[Cu(\mathbf{3})]^{1+}$ and $[Cu(\mathbf{3})]^{2+}$

An equimolar ratio of the appropriate copper salt, $[Cu^{I}(MeCN)_4](PF_6)$ or $[Cu^{II}(ClO_4)_2]\cdot 6H_2O$, and ligand **3** was stirred in acetonitrile. The mixture was stirred for 24 hours at room temperature under N_2 atmosphere. The complexes were purified by recrystallization from concentrated acetonitrile solutions by slow diethyl ether diffusion. The Cu(I) complex is reddish-orange in color and the Cu(II) complex is green. $[Cu(\mathbf{3})](PF_6)$ characterization: HRMS: $[M^+]$ = $C_{30}H_{20}F_6N_8Cu$ calculated: 669.1011; found: 669.1034. ^{1}H NMR (500 MHz, CD_3CN, with trace amount of hydrazine added): δ 8.58, 8.02, 7.90, 7.72, 7.68, 7.61, 7.47, 3.67. $[Cu(\mathbf{3})](ClO_4)_2$ characterization: elemental analysis calculated for $C_{30}H_{20}Cl_2CuF_6N_8O_8\cdot H_2O$: C 40.62, H 2.50, N 12.63; found; C 40.97, H 2.55, N 12.37.

X-Ray crystallography

Single crystals of $[Cu(\mathbf{1})(MeCN)](ClO_4)_2$ were coated with a trace of Fomblin oil and transferred to the goniometer head of a Bruker Quest diffractometer with a fixed chi angle, a sealed tube fine focus X-ray tube, single crystal curved graphite incident beam monochromator, a Photon100 CMOS area detector, and an Oxford Cryosystems low temperature device. Examination and data collection were performed with Mo Kα radiation (λ = 0.71073 Å) at 150 K. Data were collected, reflections were indexed and processed, and the files scaled and corrected for absorption using APEX3.[75] The space groups were assigned and the structures were solved by direct methods using XPREP within the SHELXTL suite of programs[76,77] and refined by full matrix least squares against F^2 with all reflections using Shelxl2018[78,79] using the graphical interface Shelxle.[80] If not specified otherwise H atoms attached to carbon atoms were positioned geometrically and constrained to ride on their parent atoms. C–H bond distances were constrained to 0.95 Å for aromatic C–H moieties and to 0.98 Å for aliphatic CH_3 moieties. U_{iso}(H) values were set to a multiple of U_{eq}(C) with 1.5 for CH_3 and 1.2 for C–H units, respectively.

Additional data collection and refinement details, including description of disorder (where present) can be found in the ESI.† Complete crystallographic data, in CIF format, have been deposited with the Cambridge Crystallographic Data Centre. CCDC 1959279† contains the supplementary crystallographic data for this paper.

Device fabrication

DSC devices were prepared as follows: TEC 10 FTO glass (10 Ω sq.$^{-1}$ sheet resistance, FTO is fluorine-doped tin oxide, purchased from Hartford Glass) was cut into 2 × 2 cm squares. The substrate was submerged in a 0.2% Deconex 21 aqueous solution and sonicated for 15 minutes at room temperature. The electrodes were then rinsed with water and sonicated in acetone for 10 minutes followed by sonication in ethanol for 10 minutes. The electrodes were next placed under UV/ozone for 15 minutes (UV-Ozone Cleaning System, Model ProCleaner by UVFAB Systems). A TiO_2 underlayer was then applied by treatment of the substrate submerged in a 40 mM $TiCl_4$ solution in water (prepared from 99.9% $TiCl_4$ between 0–5 °C) by adding $TiCl_4$ to a stirred water solution carefully dropwise. The submerged substrates (conductive side up) were heated for 30 minutes at 70 °C. After heating, the substrates were rinsed first with water and then with ethanol. Active layer TiO_2 (nano-

particle size: 38–31 nm, Greatcell, DN-GPS-30TS) was applied *via* screen printing (Sefar screen (90/230–48 W) resulting in 5.0 μm TiO_2 thickness. Scattering layer TiO_2 (particle size, >100 nm, Solaronix R/SP) was applied *via* screen printing (Sefar screen (54/137–64 W). Between each print, the substrate was heated for 7 minutes at 125 °C and the thickness was measured with a profilometer (Alpha-Step D-500 KLA Tencor). After the films were printed, the substrate was then sintered with progressive heating from 125 °C (5 minutes ramp from r. t., 5 minutes hold) to 325 °C (15 minutes ramp from 125 °C, 5 minutes hold) to 375 °C (5 minutes ramp from 325 °C, 5 minutes hold) to 450 °C (5 minutes ramp from 375 °C, 15 minutes hold) to 500 °C (5 minutes ramp from 450 °C, 15 minutes hold) using a programmable furnace (Vulcan® 3-Series Model 3–550). The cooled sintered photoanode was soaked for 30 minutes at 70 °C in a 40 mM $TiCl_4$ water solution and heated again at 500 °C for 30 minutes prior to sensitization. The complete working electrode was prepared by immersing the TiO_2 film into a room temperature 0.2 mM **Y123** dye solution in 1 : 1 (MeCN : *tert*-butanol) with 50 : 1 chenodeoxycholic acid (CDCA) : dye for 16 hours. Counter Electrodes Fabrication: Two holes were drilled in 2 × 2 cm squares of TEC 7 FTO glass (Hartford Glass) using a Dremel-4000 with Dremel 7134 Diamond Taper Point Bit under water from the conductive side through to the non-conductive side with tape on the FTO side to protect the surface. Electrodes were washed with water followed by rinsing with a 121 : 1 (v/v) mixture of EtOH/concentrated aqueous HCl, and sonication in an acetone bath for 10 minutes. Platinum was applied by slot printing a thin layer of Pt-paste (Solaronix, Platisol T/SP) with a punched Scotch tape piece on the conductive side. The electrodes were then heated at 450 °C for 10 minutes. PEDOT electrodes were made according to literature procedure.[81]

Device assembly

The photoanode and cathode were sealed with a 25 μm thick hot melt film (Surlyn, DuPont) by heating the counter electrode at 130 °C under 0.15 psi pressure for 55 seconds. Devices were completed by filling the cells with electrolyte through the pre-drilled holes in the counter electrodes, and the holes were sealed with a Surlyn pre-cut circle and a thin glass cover by heating at 130 °C under pressure 0.1 psi for 25 seconds. $[Cu(\mathbf{1})]^{2+/1+}$, $[Cu(\mathbf{2})]^{2+/1+}$ and $[Cu(\mathbf{3})]^{2+/1+}$ RS electrolytes were comprised of: 0.2 M Cu(I), 0.04 M Cu(II), 0.1 M LiTFSI, and 0.5 M TBP in acetonitrile. $[Cu(bpye)]^{2+/1+}$ electrolyte was made according to literature procedure.[82] Finally, soldered contacts were added with a MBR Ultrasonic soldering machine (model USS-9210) with solder alloy (Cerasolzer wire 1.6 mm diameter, item # CS186-150). A circular black mask (active area 0.15 cm^2) punched from black tape was used in the subsequent photovoltaic studies.

Photovoltaic characterization general information

Photovoltaic characteristics were measured using a 300 W xenon lamp (Model SF300A, SCIENCETECH Inc. Class AAA) solar simulator equipped with an AM 1.5 G filter for a less than 2% spectral mismatch. Prior to each measurement, the solar simulator output was calibrated with a KG5 filtered mono-crystalline silicon NREL calibrated reference cell from ABET Technologies (Model 15150-KG5). The current density–voltage characteristic of each cell was obtained with a Keithley digital source meter (Model 2400).

Incident photon-to-current conversion efficiency

Incident photon-to-current conversion efficiency was measured with an IPCE instrument manufactured by Dyenamo comprised of a 175 W xenon lamp (CERMAX, Model LX175F), monochromator (Spectral Products, Model CM110, Czerny-Turner, dual-grating), filter wheel (Spectral Products, Model AB301 T, fitted with filter AB3044 [440 nm high pass] and filter AB3051 [510 nm high pass]), a calibrated UV-enhanced silicon photodiode reference, and Dyenamo issued software.

Small modulated photovoltage transient measurements

Small modulated photovoltage transient measurements were carried out with a Dyenamo Toolbox (DN-AE01) instrument and software. The intensity of the LED light source (Seoul Semiconductors, Natural White, S42182H, 450 nm to 750 nm emission) is varied to modulate the device open-circuit voltage. The base light intensity was modulated by applied voltages of 2.80, 2.85, 2.90, 2.95 and 3.00 to the LED with the 3.00 V bias approaching 1 sun intensity (97% sun). The direction of illumination was from the photoanode to the counter electrode, and the device was positioned 5 cm from the LED light source. The voltage rise and decay times are fitted with a Levenberg–Marquardt fitting algorithm *via* LabView, and the electron lifetime was obtained from the averaging of rise and decay times.

Electrochemical impedance spectroscopy

Electrochemical impedance spectroscopy measurements were conducted with an impedance analyzer, potentiostat (CHI 6054E, AC Impedance technique) in the dark. EIS spectra were recorded over a frequency range of 100 mHz to 220 kHz. The applied bias voltage was set at −0.6 V, with AC amplitude of 10 mV.

Conflicts of interest

The authors declare no competing financial interest.

Acknowledgements

This material is based on work supported by the National Science Foundation under Grant No. 1757220.

References

1 A. Mishra, M. K. Fischer and P. Bauerle, *Angew. Chem., Int. Ed.*, 2009, **48**, 2474–2499.

2 A. Hagfeldt, G. Boschloo, L. Sun, L. Kloo and H. Pettersson, *Chem. Rev.*, 2010, **110**, 6595–6663.
3 T. W. Hamann and J. W. Ondersma, *Energy Environ. Sci.*, 2011, **4**, 370–381.
4 B. E. Hardin, H. J. Snaith and M. D. McGehee, *Nat. Photonics*, 2012, **6**, 162–169.
5 S. Zhang, X. Yang, Y. Numata and L. Han, *Energy Environ. Sci.*, 2013, **6**, 1443–1464.
6 A. Fakharuddin, R. Jose, T. M. Brown, F. Fabregat-Santiago and J. Bisquert, *Energy Environ. Sci.*, 2014, **7**, 3952–3981.
7 Y. Wu, W. H. Zhu, S. M. Zakeeruddin and M. Gratzel, *ACS Appl. Mater. Interfaces*, 2015, **7**, 9307–9318.
8 A. Polman, M. Knight, E. C. Garnett, B. Ehrler and W. C. Sinke, *Science*, 2016, **352**, 307.
9 J. M. Cole, G. Pepe, O. K. Al Bahri and C. B. Cooper, *Chem. Rev.*, 2019, **119**, 7279–7327.
10 Y. Saygili, M. Stojanovic, N. Flores-Díaz, S. M. Zakeeruddin, N. Vlachopoulos, M. Grätzel and A. Hagfeldt, *Inorganics*, 2019, **7**, 30.
11 M. Gorlov and L. Kloo, *Dalton Trans.*, 2008, 2655–2666.
12 B. Pashaei, H. Shahroosvand and P. Abbasi, *RSC Adv.*, 2015, **5**, 94814–94848.
13 Z. Sun, M. Liang and J. Chen, *Acc. Chem. Res.*, 2015, **48**, 1541–1550.
14 J. Wu, Z. Lan, J. Lin, M. Huang, Y. Huang, L. Fan and G. Luo, *Chem. Rev.*, 2015, **115**, 2136–2173.
15 W. Zhang, Y. Wu, H. W. Bahng, Y. Cao, C. Yi, Y. Saygili, J. Luo, Y. Liu, L. Kavan, J.-E. Moser, A. Hagfeldt, H. Tian, S. M. Zakeeruddin, W.-H. Zhu and M. Grätzel, *Energy Environ. Sci.*, 2018, **11**, 1779–1787.
16 Y. Xie, Y. Tang, W. Wu, Y. Wang, J. Liu, X. Li, H. Tian and W. H. Zhu, *J. Am. Chem. Soc.*, 2015, **137**, 14055–14058.
17 H. Ozawa, T. Sugiura, T. Kuroda, K. Nozawa and H. Arakawa, *J. Mater. Chem. A*, 2016, **4**, 1762–1770.
18 C.-Y. Chen, M. Wang, J.-Y. Li, N. Pootrakulchote, L. Alibabaei, C. H. Ngoc-le, J. D. Decoppet, J.-H. Tsai, C. Grätzel, C.-G. Wu, S. M. Zakeeruddin and M. Grätzel, *ACS Nano*, 2009, **3**, 3103–3109.
19 K. Kakiage, Y. Aoyama, T. Yano, K. Oya, J. I. Fujisawa and M. Hanaya, *Chem. Commun.*, 2015, **51**, 15894–15897.
20 M. Hu, J. Shen, Z. Yu, R. Z. Liao, G. G. Gurzadyan, X. Yang, A. Hagfeldt, M. Wang and L. Sun, *ACS Appl. Mater. Interfaces*, 2018, **10**, 30409–30416.
21 J. Cong, D. Kinschel, Q. Daniel, M. Safdari, E. Gabrielsson, H. Chen, P. H. Svensson, L. Sun and L. Kloo, *J. Mater. Chem. A*, 2016, **4**, 14550–14554.
22 Y. Saygili, M. Soderberg, N. Pellet, F. Giordano, Y. Cao, A. B. Munoz-Garcia, S. M. Zakeeruddin, N. Vlachopoulos, M. Pavone, G. Boschloo, L. Kavan, J. E. Moser, M. Gratzel, A. Hagfeldt and M. Freitag, *J. Am. Chem. Soc.*, 2016, **138**, 15087–15096.
23 M. Freitag, Q. Daniel, M. Pazoki, K. Sveinbjörnsson, J. Zhang, L. Sun, A. Hagfeldt and G. Boschloo, *Energy Environ. Sci.*, 2015, **8**, 2634–2637.
24 Y. Cao, Y. Saygili, A. Ummadisingu, J. Teuscher, J. Luo, N. Pellet, F. Giordano, S. M. Zakeeruddin, J. E. Moser, M. Freitag, A. Hagfeldt and M. Gratzel, *Nat. Commun.*, 2017, **8**, 15390.
25 Y. Cao, Y. Liu, S. M. Zakeeruddin, A. Hagfeldt and M. Grätzel, *Joule*, 2018, **2**, 1108–1117.
26 H. Michaels, I. Benesperi, T. Edvinsson, A. Muñoz-Garcia, M. Pavone, G. Boschloo and M. Freitag, *Inorganics*, 2018, **6**, 53.
27 A. Colombo, R. Ossola, M. Magni, D. Roberto, D. Jacquemin, C. Castellano, F. Demartin and C. Dragonetti, *Dalton Trans.*, 2018, **47**, 1018–1022.
28 R. Garcia-Rodriguez, R. Jiang, E. J. Canto-Aguilar, G. Oskam and G. Boschloo, *Phys. Chem. Chem. Phys.*, 2017, **19**, 32132–32142.
29 J. Li, X. Yang, Z. Yu, G. G. Gurzadyan, M. Cheng, F. Zhang, J. Cong, W. Wang, H. Wang, X. Li, L. Kloo, M. Wang and L. Sun, *RSC Adv.*, 2017, **7**, 4611–4615.
30 M. Magni, R. Giannuzzi, A. Colombo, M. P. Cipolla, C. Dragonetti, S. Caramori, S. Carli, R. Grisorio, G. P. Suranna, C. A. Bignozzi, D. Roberto and M. Manca, *Inorg. Chem.*, 2016, **55**, 5245–5253.
31 M. Magni, P. Biagini, A. Colombo, C. Dragonetti, D. Roberto and A. Valore, *Coord. Chem. Rev.*, 2016, **322**, 69–93.
32 W. L. Hoffeditz, M. J. Katz, P. Deria, G. E. Cutsail Iii, M. J. Pellin, O. K. Farha and J. T. Hupp, *J. Phys. Chem. C*, 2016, **120**, 3731–3740.
33 A. Colombo, G. Di Carlo, C. Dragonetti, M. Magni, A. O. Biroli, M. Pizzotti, D. Roberto, F. Tessore, E. Benazzi, C. A. Bignozzi, L. Casarin and S. Caramori, *Inorg. Chem.*, 2017, **56**, 14189–14197.
34 S. C. Pradhan, A. Hagfeldt and S. Soman, *J. Mater. Chem. A*, 2018, **6**, 22204–22214.
35 Y. Wang and T. W. Hamann, *Chem. Commun.*, 2018, **54**, 12361–12364.
36 Y. Saygili, M. Stojanovic, H. Michaels, J. Tiepelt, J. Teuscher, A. Massaro, M. Pavone, F. Giordano, S. M. Zakeeruddin, G. Boschloo, J.-E. Moser, M. Grätzel, A. B. Muñoz-García, A. Hagfeldt and M. Freitag, *ACS Appl. Energy Mater.*, 2018, **1**, 4950–4962.
37 Y. Zhao, J. Shen, Z. Yu, M. Hu, C. Liu, J. Fan, H. Han, A. Hagfeldt, M. Wang and L. Sun, *J. Mater. Chem. A*, 2019, **7**, 12808–12814.
38 S. Samanta and N. Lehnert, *Nat. Chem.*, 2016, **8**, 639–641.
39 E. Müller, C. Piguet, G. Bernardinelli and A. F. Williams, *Inorg. Chem.*, 1988, **27**, 849–855.
40 O. P. Anderson, J. Becher, H. Frydendahl, L. F. Taylor and H. Toftlund, *J. Chem. Soc., Chem. Commun.*, 1986, 699–701.
41 S. Knapp, T. P. Keenan, X. Zhang, R. Fikar, J. A. Potenza and H. J. Schugar, *J. Am. Chem. Soc.*, 1990, **112**, 3452–3464.
42 E. Müller, G. Bernardinelli and J. Reedijk, *Inorg. Chem.*, 1996, **35**, 1952–1957.
43 M. R. Malachowski, M. Adams, N. Elia, A. L. Rheingold and R. S. Kelly, *J. Chem. Soc., Dalton Trans.*, 1999, 2177–2182.
44 M. Reglier, C. Jorand and B. Waegell, *J. Chem. Soc., Chem. Commun.*, 1990, 1752–1755.

45 M. R. Malachowski, A. S. Kasto, M. E. Adams, A. L. Rheingold, L. N. Zakharov, L. D. Margerum and M. Greaney, *Polyhedron*, 2009, **28**, 393–397.
46 L. Chen, H. A. Dulaney, B. O. Wilkins, S. Farmer, Y. Zhang, F. R. Fronczek and J. W. Jurss, *New J. Chem.*, 2018, **42**, 18667–18677.
47 K. B. Ørnsø, E. Ö. Jónsson, K. W. Jacobsen and K. S. Thygesen, *J. Phys. Chem. C*, 2015, **119**, 12792–12800.
48 J. P. Perdew, K. Burke and M. Ernzerhof, *Phys. Rev. Lett.*, 1997, **78**, 1396.
49 J. P. Perdew, K. Burke and M. Ernzerhof, *Phys. Rev. Lett.*, 1996, **77**, 3865–3868.
50 A. D. Becke, *J. Chem. Phys.*, 1993, **98**, 5648–5652.
51 J. P. Perdew, J. A. Chevary, S. H. Vosko, K. A. Jackson, M. R. Pederson, D. J. Singh and C. Fiolhais, *Phys. Rev. B: Condens. Matter Mater. Phys.*, 1992, **46**, 6671–6687.
52 M. J. Frisch, G. W. Trucks, H. B. Schlegel, G. E. Scurseria, M. A. Robb, J. R. Cheeseman, G. Scalmani, V. Barone, B. Mennucci, A. Petersson, H. Nakatsuji, M. Caricato, X. Li, H. P. Hratchian, A. F. Izmaylov, J. Bloino, G. Zheng, J. L. Sonnenberg, M. Hada, M. Ehara, K. Toyota, R. Fukuda, J. Hasegawa, M. Ishida, T. Nakajima, Y. Honda, O. Kitao, H. Nakai, t. Vreven, J. A. Montgomery Jr., J. E. Peralta, F. Ogliaro, M. Bearpark, J. J. Heyd, E. Brothers, K. N. Kudin, V. N. Staroverov, R. Kobayashi, J. Normand, K. Raghavachari, A. Rendell, J. C. Burant, S. S. Iyengar, J. Tomasi, M. Cossi, N. Rega, J. M. Millam, M. Klene, J. E. Knox, J. B. Cross, V. Bakken, C. Adamo, J. Jaramillo, R. Gomperts, R. E. Stratmann, O. Yazyev, A. J. Austin, R. Cammi, C. Pomelli, J. W. Ochterski, R. L. Martin, K. Morokuma, V. G. Zakrzewski, G. A. Voth, P. Salvador, J. J. Dannenberg, S. Dapprich, A. D. Daniels, O. Farkas, J. B. Foresman, J. V. Ortiz, J. Cioslowski and D. J. Fox, *Gaussian09 Revision D.01*, Gaussian, Inc., Wallingford, CT, USA, 2009.
53 W. J. Hehre, R. Ditchfield and J. A. Pople, *J. Chem. Phys.*, 1972, **56**, 2257–2261.
54 F. Weigend and R. Ahlrichs, *Phys. Chem. Chem. Phys.*, 2005, **7**, 3297–3305.
55 F. Weigend, *Phys. Chem. Chem. Phys.*, 2006, **8**, 1057–1065.
56 E. Reisner, V. B. Arion, A. Eichinger, N. Kandler, G. Giester, A. J. L. Pombeiro and B. K. Keppler, *Inorg. Chem.*, 2005, **44**, 6704–6716.
57 M. H. Reineke, M. D. Sampson, A. L. Rheingold and C. P. Kubiak, *Inorg. Chem.*, 2015, **54**, 3211–3217.
58 A. J. Bard and L. R. Faulkner, *Electrochemical Methods: Fundamentals and Applications*, John Wiley & Sons, inc., New York, 2nd edn, 2001.
59 M. Urbani, M. Grätzel, M. K. Nazeeruddin and T. Torres, *Chem. Rev.*, 2014, **114**, 12330–12396.
60 A. Mishra, M. K. Fischer and P. Bäuerle, *Angew. Chem., Int. Ed.*, 2009, **48**, 2474–2499.
61 A. Y. Anderson, P. R. Barnes, J. R. Durrant and B. C. O'Regan, *J. Phys. Chem. C*, 2011, **115**, 2439–2447.
62 S. Ahmad, T. Bessho, F. Kessler, E. Baranoff, J. Frey, C. Yi, M. Gratzel and M. K. Nazeeruddin, *Phys. Chem. Chem. Phys.*, 2012, **14**, 10631–10639.
63 J. H. Yum, E. Baranoff, F. Kessler, T. Moehl, S. Ahmad, T. Bessho, A. Marchioro, E. Ghadiri, J. E. Moser, C. Yi, M. K. Nazeeruddin and M. Grätzel, *Nat. Commun.*, 2012, **3**, 631.
64 H. N. Tsao, C. Yi, T. Moehl, J. H. Yum, S. M. Zakeeruddin, M. K. Nazeeruddin and M. Grätzel, *ChemSusChem*, 2011, **4**, 591–594.
65 S. M. Feldt, P. W. Lohse, F. Kessler, M. K. Nazeeruddin, M. Gratzel, G. Boschloo and A. Hagfeldt, *Phys. Chem. Chem. Phys.*, 2013, **15**, 7087–7097.
66 S. Y. Chae, S. J. Park, O. S. Joo, Y. Jun, B. K. Min and Y. J. Hwang, *Sci. Rep.*, 2016, **6**, 30868.
67 H. Cheema, R. R. Rodrigues and J. H. Delcamp, *Energy Environ. Sci.*, 2017, **10**, 1764–1769.
68 R. R. Rodrigues, H. Cheema and J. H. Delcamp, *Angew. Chem., Int. Ed.*, 2018, **57**, 5472–5476.
69 H. Cheema and J. H. Delcamp, *Adv. Energy Mater.*, 2019, **9**, 1900162.
70 H. N. Tsao, J. Burschka, C. Yi, F. Kessler, M. K. Nazeeruddin and M. Grätzel, *Energy Environ. Sci.*, 2011, **4**, 4921.
71 S. R. Raga, E. M. Barea and F. Fabregat-Santiago, *J. Phys. Chem. Lett.*, 2012, **3**, 1629–1634.
72 Z. Ning, Y. Fu and H. Tian, *Energy Environ. Sci.*, 2010, **3**, 1170–1181.
73 H. Cheema and J. H. Delcamp, *ACS Appl. Mater. Interfaces*, 2017, **9**, 3050–3059.
74 J. Nissfolk, K. Fredin, A. Hagfeldt and G. Boschloo, *J. Phys. Chem. B*, 2006, **110**, 17715–17718.
75 S. V. A. Bruker, *APEX3 v2016.9-0, SAINT V8.37A*, Bruker AXS Inc., Madison (WI), USA, 2016, 2013/2014.
76 G. M. Sheldrick, *Acta Crystallogr., Sect. A: Found. Crystallogr.*, 2008, **64**, 112–122.
77 *V. SHELXTL suite of programs, 2000-2003, Bruker Advanced X-ray Solutions*, Bruker AXS Inc., Madison, Wisconsin, USA.
78 G. M. Sheldrick, *Acta Crystallogr., Sect. C: Struct. Chem.*, 2015, **71**, 3–8.
79 G. M. Sheldrick, *Shelxl2018*, University of Göttingen, 2018.
80 C. B. Hübschle, G. M. Sheldrick and B. Dittrich, *J. Appl. Crystallogr.*, 2011, **44**, 1281–1284.
81 H. Ellis, N. Vlachopoulos, L. Häggman, C. Perruchot, M. Jouini, G. Boschloo and A. Hagfeldt, *Electrochim. Acta*, 2013, **107**, 45–51.
82 J. Cong, D. Kinschel, Q. Daniel, M. Safdari, E. Gabrielsson, H. Chen, P. H. Svensson, L. Sun and L. Kloo, *J. Mater. Chem. A*, 2016, **4**, 14550–14554.